Article

Early Detection of Rubber Tree Powdery Mildew by Combining Spectral and Physicochemical Parameter Features

Xiangzhe Cheng [1,2,3,†], Mengning Huang [4,†], Anting Guo [1,2], Wenjiang Huang [1,2,3,*], Zhiying Cai [5,6], Yingying Dong [1,3], Jing Guo [1,3], Zhuoqing Hao [1,3], Yanru Huang [1,3], Kehui Ren [1,3], Bohai Hu [1,3], Guiliang Chen [5,6], Haipeng Su [5,6], Lanlan Li [5,6] and Yixian Liu [5,6]

1   State Key Laboratory of Remote Sensing Science, Aerospace Information Research Institute, Chinese Academy of Sciences, Beijing 100094, China; chengxiangzhe22@mails.ucas.ac.cn (X.C.); guoat@aircas.ac.cn (A.G.); dongyy@aircas.ac.cn (Y.D.); guojing211@mails.ucas.ac.cn (J.G.); haozhuoqing20@mails.ucas.ac.cn (Z.H.); huangyanru19@mails.ucas.ac.cn (Y.H.); renkehui22@mails.ucas.ac.cn (K.R.); hubohai22@mails.ucas.ac.cn (B.H.)
2   Key Laboratory of Earth Observation of Hainan Province, Hainan Aerospace Information Research Institute, Sanya 572029, China
3   University of Chinese Academy of Sciences, Beijing 100049, China
4   Faculty of Information Technology, Beijing University of Technology, Beijing 100124, China; lemon20030218@126.com
5   Yunnan Key Laboratory of Sustainable Utilization Research on Rubber Tree, Yunnan Institute of Tropical Crops, Jinhong 666100, China; caizhiyingyn@sina.com (Z.C.); chen_guiliang@163.com (G.C.); 18908815100@163.com (H.S.); lilanlan1020@163.com (L.L.); liuyixian722yn@sina.com (Y.L.)
6   National and Local Joint Engineering Research Center of Breeding and Cultivation Technology of Rubber Tree, Yunnan Institute of Tropical Crops, Jinhong 666100, China
*   Correspondence: huangwj@aircas.ac.cn
†   These authors contributed equally to this work.

Abstract: Powdery mildew significantly impacts the yield of natural rubber by being one of the predominant diseases that affect rubber trees. Accurate, non-destructive recognition of powdery mildew in the early stage is essential for the cultivation management of rubber trees. The objective of this study is to establish a technique for the early detection of powdery mildew in rubber trees by combining spectral and physicochemical parameter features. At three field experiment sites and in the laboratory, a spectroradiometer and a hand-held optical leaf-clip meter were utilized, respectively, to measure the hyperspectral reflectance data (350–2500 nm) and physicochemical parameter data of both healthy and early-stage powdery-mildew-infected leaves. Initially, vegetation indices were extracted from hyperspectral reflectance data, and wavelet energy coefficients were obtained through continuous wavelet transform (CWT). Subsequently, significant vegetation indices (VIs) were selected using the ReliefF algorithm, and the optimal wavelengths (OWs) were chosen via competitive adaptive reweighted sampling. Principal component analysis was used for the dimensionality reduction of significant wavelet energy coefficients, resulting in wavelet features (WFs). To evaluate the detection capability of the aforementioned features, the three spectral features extracted above, along with their combinations with physicochemical parameter features (PFs) (VIs + PFs, OWs + PFs, WFs + PFs), were used to construct six classes of features. In turn, these features were input into support vector machine (SVM), random forest (RF), and logistic regression (LR), respectively, to build early detection models for powdery mildew in rubber trees. The results revealed that models based on WFs perform well, markedly outperforming those constructed using VIs and OWs as inputs. Moreover, models incorporating combined features surpass those relying on single features, with an overall accuracy (OA) improvement of over 1.9% and an increase in F1-Score of over 0.012. The model that combines WFs and PFs shows superior performance over all the other models, achieving OAs of 94.3%, 90.6%, and 93.4%, and F1-Scores of 0.952, 0.917, and 0.941 on SVM, RF, and LR, respectively. Compared to using WFs alone, the OAs improved by 1.9%, 2.8%, and 1.9%, and the F1-Scores increased by 0.017, 0.017, and 0.016, respectively. This study showcases the viability of early detection of powdery mildew in rubber trees.

1. Introduction

The rubber tree (*Hevea brasiliensis*), a valuable economic crop, produces milky latex, which serves as the primary source of natural rubber. Originating in the tropical rainforests of the Amazon River basin, it thrives in tropical and subtropical regions. Powdery mildew, resulting from infestation by the pathogen *Oidium heveae Steinmann*, is among the prominent diseases impacting rubber trees [1]. It is commonly found in the spring during the period of bud break and leaf spread, primarily damaging the young leaves, shoots, and inflorescences, leading to secondary leaf fall. This results in a delayed onset of rubber tapping and significantly impacts the production of natural rubber [2]. Early on in the infectious process, rubber tree leaves begin to show a small amount of scattered radial silver-white mycelium, which can rapidly spread across the entire plantation area under suitable climatic conditions [3]. Traditional detection of powdery mildew primarily relies on experienced professionals conducting periodic leaf surveys to assess the disease's severity. However, this method is labor-intensive, lacks strong representativeness, and suffers from incomplete and untimely data submissions from some sites, diminishing its effectiveness in offering timely scientific guidance. Therefore, achieving accurate detection in the early stages of powdery mildew occurrence could effectively control its outbreak, holding significant importance for agricultural production.

In recent years, hyperspectral remote sensing technology has acquired widespread usage in crop disease detection, leveraging its benefits of swift measurements and its non-destructive nature [4,5]. After being infected by pathogens, crops typically do not exhibit obvious visual symptoms in the early stages. However, a series of physiological and biochemical changes begin to occur, leading to different spectral responses. Therefore, disease identification can be accomplished through the analysis of crop spectral reflectance. Common hyperspectral-based methods for detecting crop diseases include vegetation indices, optimal wavelengths selection from original spectra, and continuous wavelet transform (CWT), among others. Vegetation indices (VIs), by combining sensitive bands and abnormal changes in spectral response, highlight the spectral characteristics of diseases, representing a simple and effective method for characterizing spectral changes. Ashour-loo et al. measured the hyperspectral data of wheat leaves and identified three sensitive wavelengths (605 nm, 695 nm, and 455 nm) for wheat leaf rust disease [6]. Based on this, they developed two vegetation indices, LRDSI_1 and LRDSI_2, enabling the monitoring of wheat leaf rust disease. Abdulridha et al. investigated and assessed 29 vegetation indices extracted from indoor hyperspectral data of squash leaves, discovering that the water index and the photochemical reflectance index could facilitate early detection and classification of squash powdery mildew [7]. Optimal wavelength (OWs) selection, by analyzing interactions between wavelengths, extracts a small number of sensitive wavelengths from abundant spectral data as the optimal feature combination, reducing redundancy between data and amplifying spectral differences between samples. Zhou et al. utilized hyperspectral reflectance data from barley leaves and employed competitive adaptive reweighted sampling (CARS) to extract 30 feature wavelengths [8]. Coupled with linear discriminant analysis (LDA), they achieved early identification of symptoms of Magnaporthe oryzae infection in barley leaves. Guo et al. employed the successive projection algorithm (SPA) to extract six feature wavelengths sensitive to wheat stripe rust, facilitating the extraction of stripe rust lesions on wheat leaves [9]. CWT is a burgeoning spectral analysis technique that decomposes spectral data across multiple scales, enabling the capture of intricate spectral variations. Shi et al. introduced a methodology employing wavelet features (WFs) to elucidate the mechanisms associated with wheat stripe rust [10]. Zhang et al. combined

CWT with partial least squares regression using hyperspectral information from infected leaves, facilitating the evaluation of winter wheat powdery mildew [11].

Compared to spectral features, physicochemical parameter features (PFs) of crops more directly reflect the physiological and chemical changes occurring after crop infection, garnering increasing attention in crop disease detection [12,13]. Wu et al. extracted multiple PFs including chlorophyll content and LAI from hyperspectral images captured by unmanned aerial vehicles during the fruit expansion period of jujube trees and established a health assessment model based on these features [14]. Liu et al. conducted a comprehensive analysis of hyperspectral data and chlorophyll content to assess the severity of Apple mosaic virus (ApMV) infection in apple leaves at the leaf scale [15]. The above studies all utilized hyperspectral data to invert PFs. In addition, portable hand-held optical leaf-clip meters such as SPAD and Dualex, owing to their advantages of real-time, accurate, and non-destructive measurement of PFs such as chlorophyll and anthocyanin content in leaves, are also commonly employed for on-site acquisition of PFs in field experiments [16]. Sims et al. conducted the detection of cassava brown streak disease and cassava mosaic disease based on SPAD measurements, demonstrating that the utilization of SPAD devices can enhance the precision of translating disease assessments from leaf-scale to landscape-scale, consequently augmenting the sensitivity of field evaluations [17]. The above studies indicate the advantage of PFs in crop disease detection. Nevertheless, there is presently a lack of research on using PFs for detecting powdery mildew in rubber trees. Therefore, further exploration is necessary to unlock the potential of PFs in identifying rubber tree powdery mildew.

The process of crop pathogen infection leading to disease is complex. Therefore, using only a single type of feature as input may not adequately characterize the complex responses of crops to diseases. In recent years, the utilization of combined features has become prevalent in early crop disease detection owing to their exceptional detection capabilities [18,19]. Tian et al. extensively utilized the rich spectral information from a two-year dataset and selected 21 features sensitive to rice blast disease from the perspectives of individual reflectance bands, spectral indices, and wavelet coefficients [20]. These features were employed for detecting rice blast disease at asymptomatic, early, and mild-infection stages, achieving detection accuracies exceeding 66%, 80%, and 95%, respectively. Zhu et al. explored the early detection of tobacco disease through hyperspectral imaging, incorporating both spectral and texture features [21]. Their findings revealed that models integrating spectral and texture features surpassed those relying solely on spectral or texture features, achieving detection accuracies exceeding 80%. The aforementioned studies provide the foundation for our research, demonstrating the superiority of utilizing combined features in the early detection of crop diseases. However, there is currently insufficient attention given to the remote sensing early detection of powdery mildew in rubber trees using combined features, particularly the combination of spectral and physicochemical parameter features. Further research in this area is warranted.

To address this research gap, especially the limited exploration of early detection methods for powdery mildew in rubber trees and the lack of studies employing combined features incorporating physiochemical parameters for this detection, this paper employs hyperspectral reflectance data and physiochemical parameter data from rubber tree leaves as data sources to propose an effective method for the early detection of powdery mildew in rubber trees by integrating spectral and physiochemical parameter features. The specific aims of this research were (1) to assess the efficacy of VIs, OWs, and WFs individually, as well as their combinations with PFs, in the early detection of powdery mildew in rubber trees; and (2) to construct an early detection model for powdery mildew in rubber trees by merging spectral and physiochemical parameter features using machine learning techniques. This research provides valuable insights for the early detection and management of powdery mildew in rubber trees.

2. Materials and Methods

2.1. Study Area

The study area, situated in the Dai Autonomous Prefecture of Xishuangbanna, Yunnan Province, China, is part of the rubber research region of the Tropical Crops Research Institute of Yunnan Province. Its geographical coordinates are 22°2′N, 100°52′E, and it sits at an elevation of 852.2 m. The year-round climate of Xishuangbanna is warm and humid, with temperatures typically ranging from 18.9 to 23.5 °C and annual precipitation of 1214.8 to 1615.9 mm. The experiment took place from 28 February to 2 March 2023, conducted both in the field and indoors. The three field experiment sites were located in Sandashan of Jinghong City (22°3′49″N, 100°53′32″E), Ganlanba Farm (21°47′42″N, 100°46′20″E), and Dongfeng Farm (21°43′41″N, 100°44′32″E). During this period, the rubber tree phenology was mainly characterized by leaves transitioning from bronze to pale green, which represents a crucial phase for identifying and managing powdery mildew in rubber trees.

2.2. Data Acquisition

2.2.1. Collection of Leaf Reflectance Spectra

Hyperspectral reflectance data from rubber tree leaves were collected using the Field-Spec Pro FR spectrometer (ASD, Boulder, CO, USA). The device spans a spectral range from 350 to 2500 nm and provides resolutions of 3 nm and 10 nm in the respective ranges of 350 to 1000 nm and 1000 to 2500 nm [22]. To mitigate the impact of the solar zenith angle on measurement outcomes, outdoor experiments were conducted between 10:00 and 14:00 local time with clear skies. During measurements, the leaves were placed flat on a 1 m by 1 m black cloth, and the probe of the spectrometer was positioned 0.5 m directly above the leaves for spectral acquisition. Each sample underwent five measurements to determine the average leaf spectral reflectance. Before each measurement, spectral calibration was performed on a 40 cm by 40 cm $BaSO_4$ reference panel. During indoor measurements, the leaves were placed horizontally on the working surface, and each sample underwent five measurements to calculate the average leaf spectral reflectance. Before measurements, a standard white reference board was used for spectrum calibration, and recalibrations were conducted every 10 to 20 min. Finally, precise spectral reflectance data were acquired, and the spectral curve was resampled to ensure a precision of 1 nm.

Samples were categorized according to the size of lesions and the visual appearance of rubber tree leaves when gathering leaf hyperspectral reflectance data, following the technical guidelines for predicting powdery mildew in rubber trees established in China in 2015 (NY/T1089-2015) [23]. Healthy (H) leaves exhibited no disease lesions, while leaves with early-stage disease (E) had lesions covering less than one-eighth of the total leaf area (Figure 1). A total of 263 leaf samples' spectral reflectance data were collected, comprising 152 H and 111 E samples. The specific sample distribution is shown in Table 1.

Figure 1. Examples of rubber tree leaves: (**a**) healthy; (**b**) early.

Table 1. Sample distribution was obtained at each experimental site.

Experimental Site	Number of Field Survey Samples		
	Healthy	Early	Sum
Sanda Mountain	43	21	64
Ganlanba Farm	30	30	60
Dongfeng Farm	29	10	39
Indoor Laboratory	50	50	100

2.2.2. Collection of Leaf Physicochemical Parameters

The leaf physicochemical parameter measurements were performed using the Dualex 4 (Force-A, Orsay, France), a portable optical leaf-clip meter capable of non-destructively and accurately evaluating chlorophyll and epidermal flavonol content [24]. During the measurement process, five measurements were taken at positions 1/3 (upper), 1/2 (middle), and 2/3 (lower) from the leaf tip for each sample, with the average subsequently calculated (Figure 2). The measurement results were displayed in units of $\mu g/cm^2$. Chlorophyll and anthocyanin content were measured and selected as the physicochemical parameters.

Figure 2. Physicochemical parameter measurement of rubber tree leaves.

2.3. Feature Extraction and Analysis

Figure 3 shows the flowchart for identifying rubber tree powdery mildew using spectral and physicochemical parameter features (VIs, OWs, WFs, and their combinations with PFs). The process comprises three steps: (1) collection of hyperspectral reflectance data and physicochemical parameter data of rubber tree leaves; (2) extraction of spectral and physicochemical parameter features (VIs were chosen using the ReliefF algorithm, OWs were selected via CARS, WFs were derived through PCA dimensionality reduction on significant wavelet energy coefficients, and PFs were obtained through measurements using the Dualex 4); (3) utilization of machine learning models to establish detection models employing various features, with model performance assessed through confusion matrices, overall accuracy, and F1-Score.
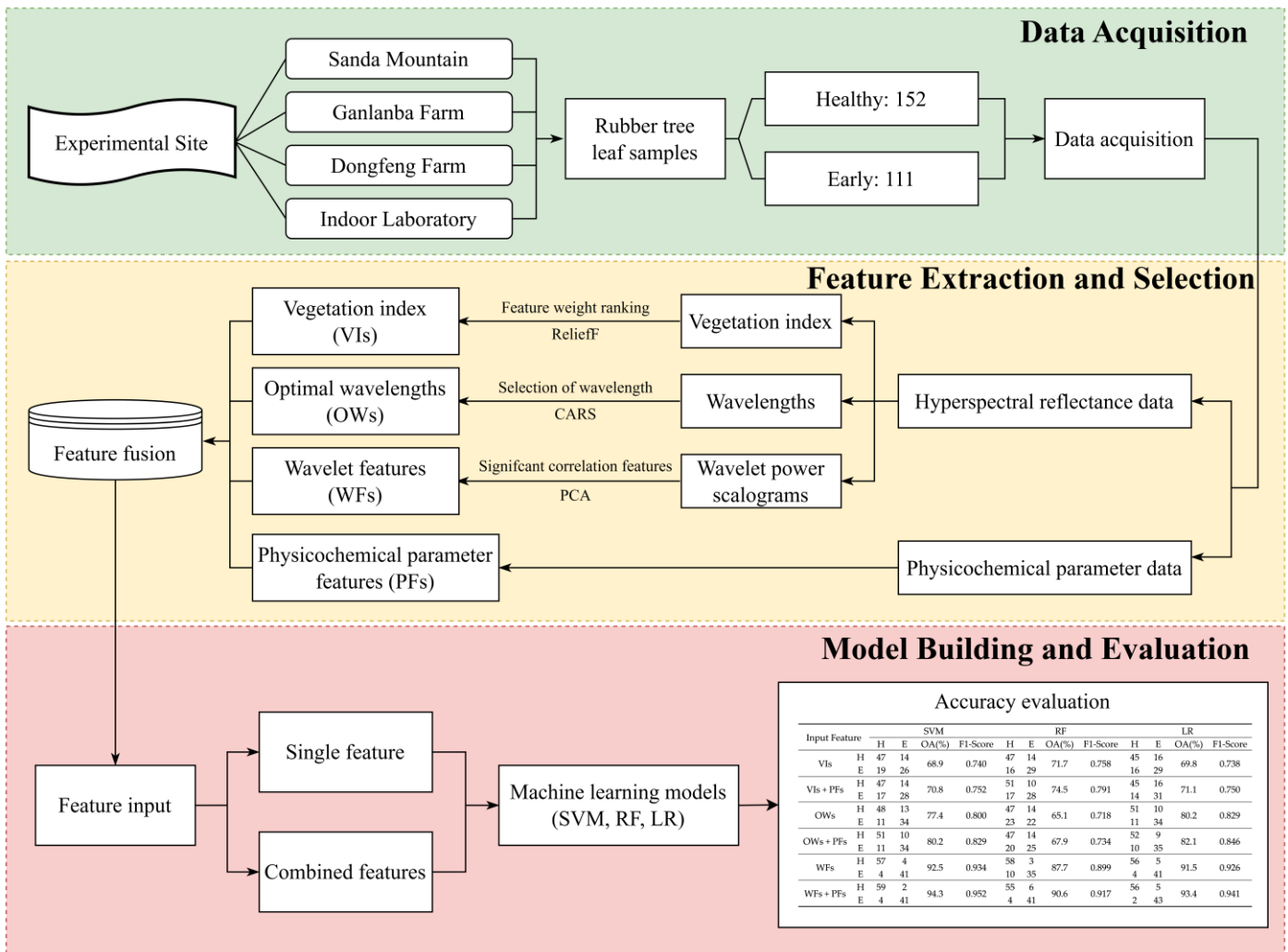
Figure 3. Flowchart of data analysis and processing.

2.3.1. Vegetation Indices Extraction and Selection

Vegetation indices play a crucial role in enhancing spectral disparities by combining and transforming wavebands, making them extensively utilized in crop disease remote sensing detection studies. In this research, we curated 39 VIs associated with pigment, structure, physiology, and water content from the pertinent literature for the early detection of powdery mildew in rubber trees, drawing upon previous studies. Table 2 presents a detailed summary of these 39 features, complete with definitions, descriptions, and references.

Table 2. Vegetation indices selected in the study.

Category	Index/Spectral Feature	Definition	Description or Formula	Reference
Pigment	ARI	Anthocyanin reflectance index	$(R_{550})^{-1} - (R_{700})^{-1}$	[25]
	$Ant_{Gitelson}$	Anthocyanin (Gitelson)	$(1/R_{550} - 1/R_{700}) \times R_{780}$	[25]
	CI_{green}	Green chlorophyll index	$(R_{750} - R_{550})/R_{550}$	[25]
	$CI_{red-edge}$	Red-edge chlorophyll index	$(R_{750} - R_{705})/R_{705}$	[26]
	CARI	Chlorophyll absorption ratio index	$(\lvert (a \times 670 + R_{670} + b) \rvert /(a^2 + 1)^{1/2}) \times (R_{700}/R_{670})$ $a = (R_{700} - R_{550})/150, b = R_{550} - (a \times 550)$	[27]

Category	Index/Spectral Feature	Definition	Description or Formula	Reference
Pigment	TCARI	Transformed chlorophyll absorption and reflectance index	$3 \times [(R_{700} - R_{670}) - 0.2 \times (R_{700} - R_{500})]/(R_{700}/R_{670})$	[28]
	MCARI	Modified chlorophyll absorption ratio index	$[(R_{701} - R_{671}) - 0.2 \times (R_{701} - R_{549})]/(R_{700}/R_{670})$	[29]
	NRI	Nitrogen reflectance index	$(R_{570} - R_{670})/(R_{570} + R_{670})$	[30]
	NPCI	Normalized pigment chlorophyll index	$(R_{680} - R_{430})/(R_{680} + R_{430})$	[31]
	PSSRa	Pigments specific simple ratio a	R_{800}/R_{680}	[32]
	PSSRb	Pigments specific simple ratio b	R_{800}/R_{635}	[32]
	PRI	Photochemical/physiological reflectance index	$(R_{531} - R_{570})/(R_{531} + R_{570})$	[33]
	PSRI	Plant senescence reflectance Index	$(R_{680} - R_{500})/R_{750}$	[34]
	PPR	Plant pigment ratio	$(R_{550} - R_{450})/(R_{550} + R_{450})$	[35]
	RGI	Red green index	R_{690}/R_{550}	[36]
	RARSa	Ratio analysis of reflectance spectra a	R_{675}/R_{700}	[37]
	RARSb	Ratio analysis of reflectance spectra b	$R_{675}/(R_{700} \times R_{650})$	[37]
	RARSc	Ratio analysis of reflectance spectra c	R_{760}/R_{500}	[37]
	OSAVI	Optimized soil-adjusted vegetation index	$(1 + 0.16) \times (R_{800} - R_{670})/(R_{800} + R_{670} + 0.16)$	[38]
	SIPI	Structure insensitive pigment index	$(R_{800} - R_{445})/(R_{800} + R_{680})$	[31]
Structure	NDVI	Normalized difference vegetation index	$(R_{800} - R_{670})/(R_{800} + R_{670})$	[39]
	NBNDVI	Narrow-band normalized Difference vegetation index	$(R_{850} - R_{680})/(R_{850} + R_{680})$	[40]
	ReNDVI	Red-edge normalized difference vegetation index	$(R_{750} - R_{705})/(R_{750} + R_{705})$	[41]
	GNDVI	Green normalized difference vegetation index	$(R_{750} - R_{540} + R_{570})/(R_{750} + R_{540} - R_{570})$	[42]
	GI	Greenness index	R_{554}/R_{677}	[36]
	SR	Simple ratio	R_{900}/R_{680}	[43]
	TVI	Triangular vegetation index	$0.5 \times [120(R_{750} - R_{550}) - 200(R_{670} - R_{550})]$	[44]
	MTVI	Modified triangular vegetation index	$1.2 \times [1.2(R_{800} - R_{550}) - 2.5(R_{670} - R_{550})]$	[45]
	RVSI	Red-edge vegetation stress Index	$[(R_{712} + R_{752})/2] - R_{732}$	[46]
Physiology	FRI1	Fluorescence ratio index 1	R_{690}/R_{630}	[47]
	FRI2	Fluorescence ratio index 2	R_{750}/R_{800}	[48]
	FRI3	Fluorescence ratio index 3	R_{690}/R_{600}	[49]
	FRI4	Fluorescence ratio index 4	R_{740}/R_{800}	[49]
	FCI	Fluorescence curvature index	$R_{683}^2/(R_{675} \times R_{691})$	[47]
	mRESR	Modified red-edge simple ratio index	$(R_{750} - R_{445})/(R_{705} + R_{445})$	[50]
	NPQI	Normalized Pheophytization Index	$(R_{415} - R_{435})/(R_{415} + R_{435})$	[51]
	PhRI	Physiological reflectance index	$(R_{550} - R_{531})/(R_{531} + R_{550})$	[33]
Water content	WI	Water Index	R_{900}/R_{970}	[52]
	WSCT	Water Stress and Canopy Temperature	$(R_{970} - R_{850})/(R_{970} + R_{850})$	[53]

Note: Rx represents the reflectance at a wavelength of x nm.

The aforementioned four types of vegetation index features may not all contribute to early detection. Reducing redundancy and selecting optimal features will enhance the model's accuracy. Therefore, the ReliefF algorithm was utilized in this study to compute the weight of each feature, retaining a small number of important features.

The ReliefF algorithm is widely employed as a feature weighting method, assigning distinct weights to features depending on their correlation with the classes [54]. Features with weights below a specific threshold are eliminated, making this approach suitable for handling data with two or more classes. The algorithm first chooses a sample *R* at random from the training sample set *D*, then retrieves *k* nearest neighbor samples *H* from the set of samples belonging to the same class as *R*, and *k* nearest neighbor samples *M* from the set of samples belonging to different classes than *R*. Subsequently, it updates the weight of each feature. The following formula is used to determine the feature weight:

$$W[A] = W[A] - \sum_{j=1}^{k} diff(A, R_i, H_j)/mk + \sum_{C \neq class(R_i)} \left[\frac{P(C)}{1 - P(class(R_i))} \sum_{j=1}^{k} diff(A, R_i, M_j(C)) \right]/mk, \quad (1)$$

where $diff(A, R_i, H_j)$ represents the Euclidean distance between sample R_i and H_j on feature *A*; $class(R_i)$ denotes the class label to which sample point R_i belongs; $P(C)$ denotes the probability of occurrence of class *C*; $P(class(R_i))$ denotes the probability of occurrence of the random sample *R*; and *m* denotes the number of sampling times.

2.3.2. Optimal Wavelengths Selection

Rubber tree leaf hyperspectral reflectance data contains rich spectral information, which aids in disease identification. The original spectral data cover a range from 350 to 2500 nm, with a total of 2151 wavelengths. Due to the data's high dimensionality, spectral redundancy and collinearity exist, which not only increase the complexity of the models but also affect their computational efficiency. Therefore, it is essential to extract the sensitive wavelengths for powdery mildew before conducting early disease detection, to diminish the dimensionality of the original spectral information, and to amplify the spectral disparities between samples. For this study, the OWs were chosen using the CARS algorithm.

The CARS algorithm [55], rooted in the Darwinian principle of "survival of the fittest", is an iterative statistical information-based method used for selecting variables, widely utilized for selecting characteristic spectral wavelengths in crop disease detection. This algorithm integrates Monte Carlo sampling with an exponential decay function in the partial least squares (PLS) model. It retains wavelength points with larger absolute regression coefficients in the PLS while discarding those with smaller weights. Through cross-validation, it identifies the subset of wavelength variables with the lowest root mean square error of cross-validation (RMSECV) as the best feature wavelengths.

2.3.3. Continuous Wavelet Transform and Features Extraction

CWT [56] is a signal processing technique rooted in the Fourier transform, allowing for the simultaneous analysis of signals in both the frequency and time domains. Utilizing CWT, the correlation analysis of original spectral curves and Gaussian functions at various positions and scales produces a set of continuous wavelet energy coefficients. As a newly emerging spectral analysis approach, it has been applied to the detection and identification of crop diseases.

The principle of CWT involves transforming hyperspectral reflectance data $f(\lambda)$ into a set of wavelet coefficients through the application of a mother wavelet function. Continuous wavelets $\psi_{a,b}(\lambda)$ are obtained by shifting and scaling the mother wavelet function $\psi(\lambda)$, with a general form as follows:

$$\psi_{a,b}(\lambda) = \frac{1}{\sqrt{a}} \psi\left(\frac{\lambda - b}{a}\right), \quad (2)$$

where "*a*" denotes the scaling factor, indicating the width of the wavelet, while "*b*" represents the shifting factor, signifying the position of the wavelet. The output during the transformation process is as follows [57]:

$$W_f(a,b) = \int_{-\infty}^{+\infty} f(\lambda)\psi_{a,b}(\lambda)d\lambda, \tag{3}$$

where $W_f(a,b)$ represents the wavelet coefficients that constitute a scalogram; $f(\lambda)$ denotes the reflectance spectrum, $\lambda = 1, 2, \ldots, m$, with m representing the number of bands—here, we set m as 2151. We selected the Mexican hat wavelet (mexh) as the foundational mother wavelet function due to its analogous vegetation absorption properties [58]. To optimize computation while maintaining the effectiveness of CWT, we focused on wavelet powers at specific scales known as dyadic scales (i.e., 2^n, n = 1, 2, ..., 10) [59].

In this study, based on CWT, we conducted a correlation analysis between the calculated wavelet energy coefficients and disease. Multiple significant results were observed across various wavebands and scales. Then, using principal component analysis (PCA) to decrease the dimensionality of the significant results relying on specific contribution rates, the resulting features from this procedure are called WFs. MATLAB 2016a was employed for all analyses of CWT.

2.4. Model Construction

In this study, the extracted VIs, OWs, WFs, and their combinations with PFs (VIs + PFs, OWs + PFs, WFs + PFs) were employed as feature variables. Six classes of feature variables were combined with support vector machine (SVM), random forest (RF), and logistic regression (LR) to establish early detection models for rubber tree powdery mildew.

SVM, a supervised learning algorithm [60], employs a kernel function to implicitly transform vectors of inputs into a high-dimensional feature space [61]. Subsequently, it seeks the best hyperplane in this feature space to accurately classify data, allowing for the modeling and classification of intricate data relationships [62]. SVM efficiently mitigates overfitting and has exceptional performance with small sample numbers and in high-dimensional spaces. Even when faced with limited training data, it is still capable of producing robust models. RF is a classifier rooted in bagging ensemble learning [63] that consists of a collection of independent, unpruned decision trees. Through random sampling with replacement, multiple sample sets are generated, and classification trees are built via a fully split method. A majority vote of the classifications from each individual binary decision tree determines the final classification result. It demonstrates relatively simple parameter tuning, good anti-overfitting characteristics, and increased robustness. LR is a classical supervised learning algorithm [64]. Assuming data follows a Bernoulli distribution, LR utilizes the Sigmoid function to constrain the results of linear regression within the (0,1) interval, representing the probability of a sample belonging to a certain class. By maximizing the likelihood function using gradient descent to solve parameters, LR achieves the objective of classifying data. LR is characterized by its simplicity, good interpretability, low computational cost, robustness to small noise in the data, and immunity to minor multicollinearity effects.

2.5. Accuracy Assessment

In order to more thoroughly assess the precision and stability of the models mentioned above, the study employed a 60:40 stratified sampling on the original dataset, dividing it into 60% for the training set and 40% for the testing set based on sample categories. The grid search method was utilized for hyperparameter tuning on the training set. The models were trained and validated using k-fold cross-validation, where the dataset was randomly partitioned into five folds. In each iteration, four folds were allocated for training and one fold was set aside for validation. To ensure comprehensive assessment, this procedure was carried out five times, with each fold acting as the validation set once. Ultimately, model performance was depicted by computing the average of evaluation metrics. The optimized

models were then tested on the testing set, and a confusion matrix was created utilizing true positives (TP), false positives (FP), true negatives (TN), and false negatives (FN), with overall accuracy (OA) computed as an evaluation metric to gauge model performance. Given the mild data imbalance, F1-Score was also incorporated into the study to provide a more comprehensive evaluation. The Python machine learning library scikit-learn version 0.24.2 was utilized for both model development and data analysis [65].

3. Results

3.1. Spectral and Physiological Responses of Rubber Tree Powdery Mildew

The elucidation of the spectral and physicochemical response mechanisms of rubber tree powdery mildew leaves forms the basis for detecting rubber tree powdery mildew using spectral and physicochemical parameter features. Figure 4a,b present the average spectral reflectance curves of healthy and early-stage rubber tree leaf samples, along with the spectral reflectance ratio between the two. The spectral reflectance curves of healthy and early-stage samples generally exhibit a similar trend, exhibiting reflection peaks near 550 nm and absorption troughs near 670 nm in the visible light region, followed by a sharp increase after 700 nm, stabilizing at a plateau of reflection shoulder around 1000 nm, and subsequently showing moisture absorption bands at 1450 nm and 1950 nm in the near-infrared region. Simultaneously, the ratio of reflectance between healthy and early-stage samples indicates that the overall spectral reflectance of early-stage diseased samples is slightly lower than that of healthy samples, with minor differences observed only in the visible light region from 400 to 670 nm and near 1950 nm in the near-infrared region, as well as beyond 2400 nm. The possible reasons for these differences may be as follows: The spectral reflectance in the visible region is primarily associated with leaf pigments [66]. Infection with powdery mildew can lead to chlorotic and necrotic leaf surfaces, causing a decrease in chlorophyll content and thus reducing leaf reflectance in the visible region. The near-infrared region of reflectance is predominantly affected by the internal leaf structure, involving water absorption, proteins, and carbohydrates [67]. Powdery mildew infection disrupts the internal and surface structures of leaves, increasing water loss and consequently decreasing near-infrared reflectance.
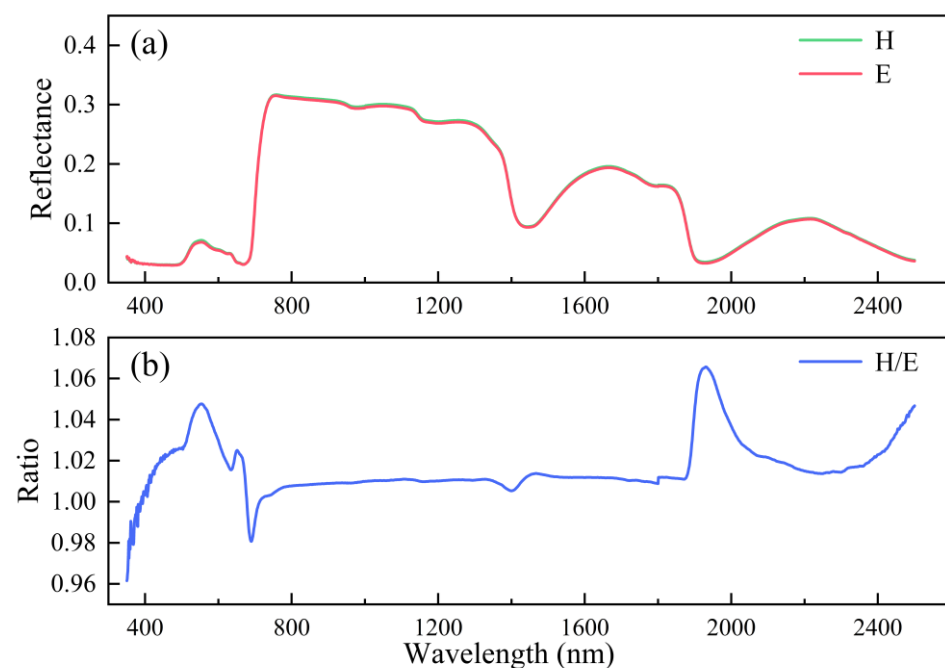

Figure 4. (**a**) Average spectral reflectance curves of healthy and early-stage diseased samples and (**b**) spectral reflectance ratio between the two.

The spectral changes in the early stages of powdery mildew infection are relatively subtle, making early detection challenging. In contrast, the response of physicochemical parameters exhibits a more rapid response. The changes in leaf physicochemical parameters are illustrated in Figure 5. The chlorophyll content of leaves shows a decreasing trend, while the anthocyanin content shows an increasing trend.
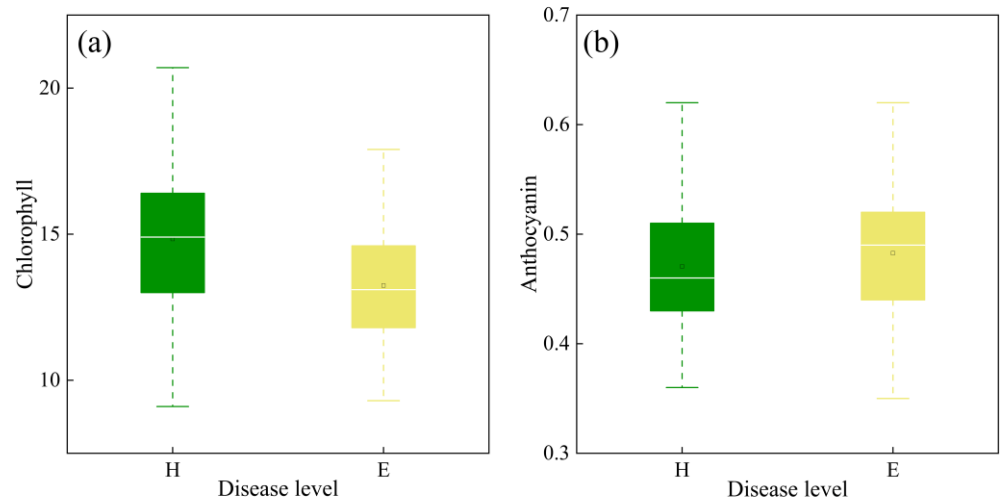

Figure 5. Physiochemical parameter responses: (**a**) chlorophyll; (**b**) anthocyanin.

3.2. Optimal Feature Extraction Results for Rubber Tree Powdery Mildew

3.2.1. Vegetation Indices

The weights of each feature were computed using the ReliefF algorithm, as illustrated in Figure 6. With a threshold of 0.03, a total of nine VIs (NPCI, PRI, PSRI, GNDVI, FRI1, FRI3, FRI4, WI, and WSCT) with high weights were selected for model construction and further identification. Among these, NPCI, PRI, and PSRI are related to leaf pigment deposition, GNDVI is sensitive to leaf cell structure, FRI1, FRI2, and FRI4 are associated with leaf physiological responses, while WI and WSCT are both correlated with leaf moisture content.
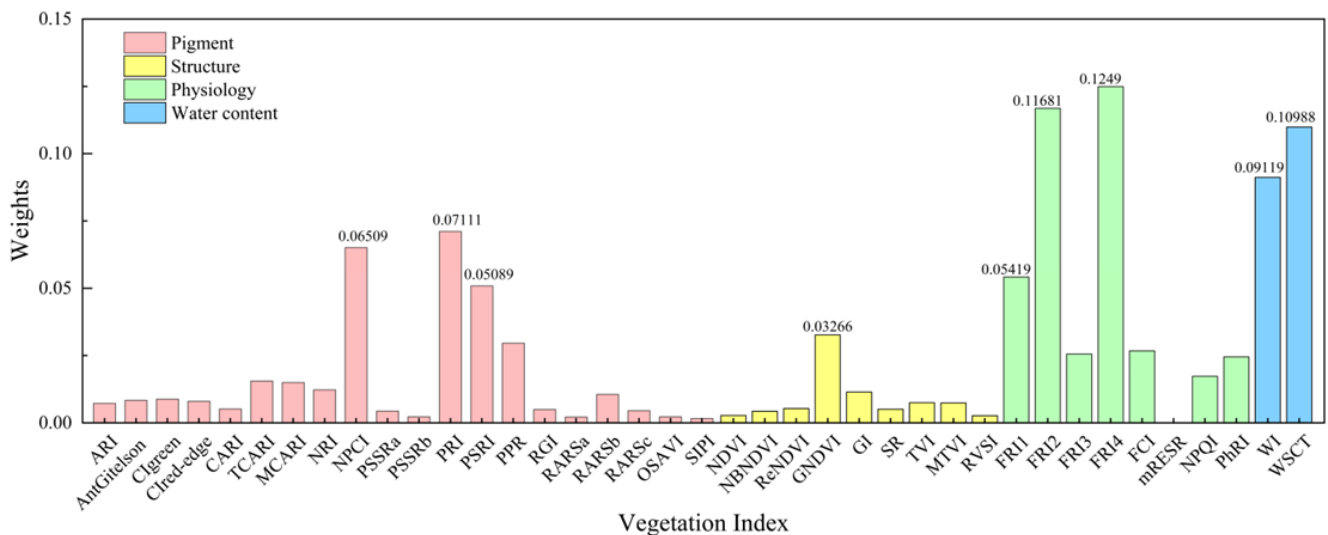

Figure 6. The weights of VIs obtained by ReliefF.

3.2.2. Optimal Wavelengths

Due to the stochastic nature of CARS sampling, this study ran the code 100 times to select the wavelength combination with the minimum RMSECV as the OWs. The process of selecting the OWs and the distribution of the selected wavelengths are illustrated in

Figure 7. As shown in Figure 7b, the lowest RMSECV value was observed when the Monte Carlo sampling was at the 31st iteration, indicating that information irrelevant to rubber tree powdery mildew detection had been removed. However, after the 31st iteration, the RMSECV gradually increased, suggesting the elimination of wavelength bands sensitive to rubber tree powdery mildew detection. Consequently, the 25 wavelength combinations obtained from the 31st iteration were selected as the feature wavelength variables, as illustrated in Figure 7c. These selected wavelengths predominantly reside in regions where there is a significant disparity between the spectral curves of samples in the visible and near-infrared regions. The proportion of the selected OWs to the total number of bands is 1.16%, significantly reducing the redundancy of the spectral dataset.
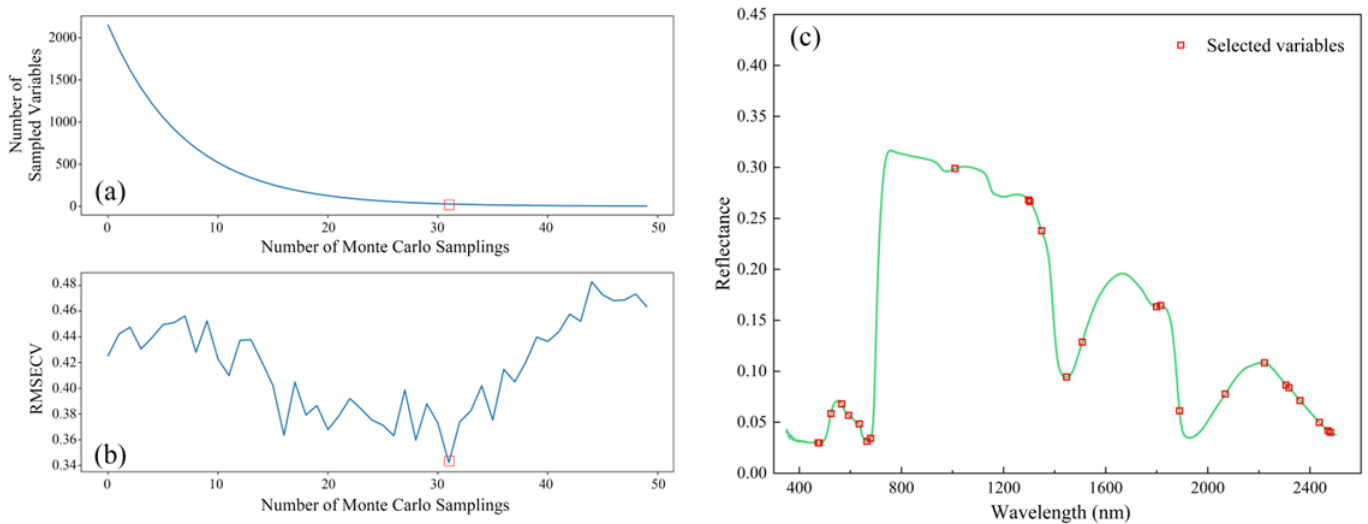

Figure 7. CARS results: (**a**) variation in the number of selected features; (**b**) variation in RMSECV; (**c**) selected wavelengths.

3.2.3. Wavelet Features

In order to determine the presence of significant correlations between the two variables, the study computed p-values to assess the link between wavelet energy coefficients across various scales and disease. Features demonstrating statistically significant correlations ($p < 0.05$) were retained, yielding 64 significant features. Dimensionality reduction through PCA was subsequently implemented on these features, aiming for a cumulative contribution rate of 90%. This process selected a total of 24 features, as illustrated in Figure 8.
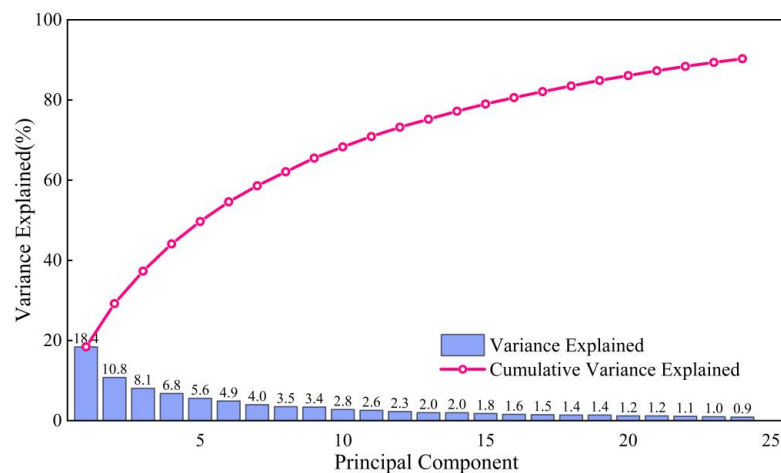

Figure 8. PCA feature contribution rate distribution.

3.3. Comparison of the Performance of Models with Different Features

Table 3 provides a summary of the confusion matrices, OAs, and F1-Scores of the early detection models constructed by combining different features with three machine learning classification methods. When employing the selected nine VIs with higher weights (NPCI, PRI, PSRI, GNDVI, FRI1, FRI3, FRI4, WI, and WSCT) as inputs, the detection models constructed using SVM, RF, and LR algorithms exhibited OAs of 68.9%, 71.6%, and 69.8%, and F1-Scores of 0.740, 0.758, and 0.738, respectively, indicating suboptimal performance for early detection of powdery mildew. Using OWs as input achieved detection accuracy exceeding 80% and F1-Score exceeding 0.8 for LR models but yielded poorer results for the RF model, demonstrating the feasibility of early detection of rubber tree powdery mildew using OWs. Compared to the full set of wavelengths, the input variables were reduced by 98.84%, resulting in a significant enhancement in modeling speed. Employing WFs as input yielded promising results, with detection rates exceeding 90%, the detection accuracy reached 92.5% and the F1-Score reached 0.934 when using the SVM model, far surpassing models constructed using VIs and OWs as inputs. For the same type of input features, models based on SVM, RF, and LR achieved the highest OAs when using WFs, VIs, and OWs as inputs, respectively. Different classification algorithms have distinct mechanisms; thus, selecting an appropriate classification algorithm to construct detection models has a significant impact on improving the accuracy of crop disease detection.

Table 3. Model accuracy for powdery mildew early detection based on different features and algorithms.

Input Feature		SVM				RF				LR			
		H	E	OA(%)	F1-Score	H	E	OA(%)	F1-Score	H	E	OA(%)	F1-Score
VIs	H	47	14	68.9	0.740	47	14	71.7	0.758	45	16	69.8	0.738
	E	19	26			16	29			16	29		
VIs + PFs	H	47	14	70.8	0.752	51	10	74.5	0.791	45	16	71.1	0.750
	E	17	28			17	28			14	31		
OWs	H	48	13	77.4	0.800	47	14	65.1	0.718	51	10	80.2	0.829
	E	11	34			23	22			11	34		
OWs + PFs	H	51	10	80.2	0.829	47	14	67.9	0.734	52	9	82.1	0.846
	E	11	34			20	25			10	35		
WFs	H	57	4	92.5	0.934	58	3	87.7	0.899	56	5	91.5	0.926
	E	4	41			10	35			4	41		
WFs + PFs	H	59	2	94.3	0.952	55	6	90.6	0.917	56	5	93.4	0.941
	E	4	41			4	41			2	43		

Simultaneously, the OAs and F1-Scores of the VIs + PFs, OWs + PFs, and WFs + PFs combined feature schemes were superior to those of models based on single features. Among them, the model combining WFs and PFs performed the best, achieving OAs of 94.3%, 90.6%, and 93.4% and F1-Scores of 0.952, 0.917, and 0.941 on the SVM, RF, and LR algorithms, respectively. Compared to using WFs alone as inputs, the OAs increased by 1.9%, 2.8%, and 1.9%, and the F1-Scores increased by 0.017, 0.017, and 0.016, respectively. Moreover, the enhancement in OA for the VIs + PFs and OWs + PFs models also surpassed 1.9%.

The above results demonstrate that models combining spectral and physiochemical parameter features outperform those based on single-feature models, highlighting the potential of PFs for early disease detection. Among all early detection models, the combination of WFs + PFs with SVM demonstrates the highest performance, achieving an OA of 94.3% and an F1-Score of 0.952. This may be attributed to the relatively subtle spectral changes in the early stages of powdery mildew infection. While the combination of bands enhances the amplification of spectral differences, the multiscale decomposition

generated by CWT at various positions provides finer spectral variations across multiple frequency regions, yielding more detailed information. In addition, when combined with PFs measured by experimental instruments, it exhibits a more rapid response.

4. Discussion

This study presents a novel model for the early detection of powdery mildew in rubber trees. It combines WFs and PFs along with SVM, which marks the first instance of integrating remote sensing technology for the early detection of powdery mildew in rubber trees. The optimal early detection model achieved an OA of 94.3% and an F1-Score of 0.952, demonstrating the substantial potential of integrating WFs and PFs for the early detection of rubber tree powdery mildew.

Hyperspectral data cover a wide range of wavelengths, providing abundant spectral information. However, this also leads to a significant amount of redundancy in the process of constructing spectral features through band combination transformation. Therefore, the selection of spectral feature variables is crucial for making model detection more efficient and improving classification accuracy. In this study, we employed the ReliefF algorithm, CARS, and PCA to select sensitive features. VIs selected using the ReliefF algorithm achieved an OA of 71.7% and an F1-Score of 0.758, indicating suboptimal performance for early detection of powdery mildew. OWs selected using CARS attained a detection accuracy of 80.2% and F1-Score of 0.829 in the LR model, with selected wavelengths predominantly located in regions where there is a significant disparity between the spectral curves of samples in the visible and near-infrared regions. These wavelengths accounted for only 1.16% of all bands, demonstrating the effectiveness and feasibility of using OWs for early detection of rubber tree powdery mildew. Previous studies have also utilized CARS to select OWs for crop disease detection, achieving promising results [68]. The detection accuracy of the model based on WFs reached 92.5%, representing approximately 20.8%- and 12.3%-higher accuracy compared to models based on VIs and OWs, respectively. This may be attributed to the relatively subtle spectral changes in the early stages of powdery mildew disease. The multiscale decomposition of spectral information by CWT at different positions allows for a more sensitive capture of spectral variations associated with moisture, pigments, morphology, and structure caused by powdery mildew. Additionally, integrating PCA helps to select the best positions and scales by reducing the complexity of the data.

Many previous studies have primarily utilized spectral features for powdery mildew identification, while this study focuses on integrating spectral features with physiochemical parameter features. The proposed models based on feature combinations (VIs + PFs, OWs + PFs, and WFs + PFs) achieved higher accuracy compared to models solely based on spectral features. For the combination of WFs and PFs, the OA increased by 1.9% and the F1-Score increased by 0.017 compared to using WFs alone as inputs. Additionally, the models combining VIs, OWs, and PFs all showed improvements in OA exceeding 1.9% and F1-Score exceeding 0.012. This demonstrates the potential of PFs as complementary features to enhance early disease detection accuracy. This may be attributed to the relatively subtle spectral changes in the early stages of the disease, where PFs exhibit more rapid responses to changes. Although PFs contributed to the model accuracy improvement, the enhancement was modest, possibly due to the limited selection of features, which only included chlorophyll and anthocyanin. Future research will explore different methods to extract additional PFs from leaves to construct superior rubber tree powdery mildew early detection models.

Our study combined WFs with PFs to achieve early detection of rubber tree powdery mildew at the leaf scale, laying the groundwork for detecting powdery mildew at larger scales such as canopy level. In recent times, the swift advancements in unmanned aerial vehicle (UAV) technology have made significant progress in applications related to pest and disease detection [69,70]. In comparison to proximal spectral measurement devices, UAVs equipped with hyperspectral imaging systems can rapidly and non-invasively capture hyperspectral images of entire rubber tree farms, facilitating deeper investigation into

canopy structure, texture, and other information. Therefore, in future research, integrating spectral and physiochemical parameter features obtained from UAV-acquired hyperspectral images and delving deeper into canopy structure, texture, and other information concerning rubber trees is anticipated to notably enhance the efficacy and precision of early detection for rubber tree powdery mildew.

5. Conclusions

In this study, leveraging hyperspectral data and physiochemical parameters of rubber tree powdery mildew, we employed the ReliefF algorithm, CARS, and CWT to extract VIs, OWs, and WFs from spectral characteristics, respectively. These features were combined with PFs and utilized to construct early detection models for rubber tree powdery mildew using SVM, RF, and LR methods. The conclusions drawn are as follows, based on the obtained results: Upon powdery mildew infection, chlorophyll content in rubber tree leaves exhibited an increasing trend, while anthocyanin content showed a decreasing trend. The overall spectral reflectance of early disease samples was slightly lower than that of healthy samples, with minor differences observed only in the visible range (400–670 nm) and near-infrared regions around 1950 nm and beyond 2400 nm. Models based on WFs demonstrated excellent performance, achieving identification rates exceeding 90%. The SVM model, in particular, exhibited a detection accuracy of 92.5%, surpassing models constructed with VIs and OWs as inputs. Additionally, models based on combined features outperformed those based on single features. The model combining WFs and PFs showed the best performance, achieving OAs of 94.3%, 90.6%, and 93.4%, and F1-Scores of 0.952, 0.917, and 0.941 on SVM, RF, and LR models, respectively. Compared to using WFs alone as inputs, the OAs increased by 1.9%, 2.8%, and 1.9%, and the F1-Scores increased by 0.017, 0.017, and 0.016, respectively. Additionally, the models combining VIs, OWs, and PFs all showed improvements in OA exceeding 1.9% and in F1-Score exceeding 0.012. Among all early detection models, the model combining WFs and PFs with SVM exhibited the best performance, achieving an OA of 94.3% and an F1-Score of 0.952. This demonstrates the effectiveness of integrating wavelet features and physiochemical parameter features for the early detection of rubber tree powdery mildew. Additionally, it lays the groundwork for larger-scale detection, such as at the canopy level. In future studies, we will explore the combination of spectral and physicochemical parameter characterization of hyperspectral images acquired using UAV technology for application in the early disease detection of rubber tree powdery mildew at the field scale.

References

1. Liyanage, K.K.; Khan, S.; Mortimer, P.E.; Hyde, K.D.; Xu, J.; Brooks, S.; Ming, Z. Powdery Mildew Disease of Rubber Tree. *For. Pathol.* **2016**, *46*, 90–103. [CrossRef]
2. Limkaisang, S.; Kom-un, S.; Takamatsu, S.; Furtado, E.L.; Liew, K.W.; Salleh, B.; Sato, Y. Molecular Phylogenetic and Morphological Analyses of Oidium Heveae, a Powdery Mildew of Rubber Tree. *Mycoscience* **2005**, *46*, 220–226. [CrossRef]
3. Liyanage, S.; Jacob, C.K. Diseases of Economic Importance in Rubber. In *Developments in Crop Science*; Elsevier: Amsterdam, The Netherlands, 1992; Volume 23, pp. 324–359.
4. Thomas, S.; Kuska, M.T.; Bohnenkamp, D.; Brugger, A.; Alisaac, E.; Wahabzada, M.; Behmann, J.; Mahlein, A.-K. Benefits of Hyperspectral Imaging for Plant Disease Detection and Plant Protection: A Technical Perspective. *J. Plant Dis. Prot.* **2018**, *125*, 5–20. [CrossRef]
5. Zhang, J.C.; Pu, R.; Wang, J.; Huang, W.; Yuan, L.; Luo, J. Detecting Powdery Mildew of Winter Wheat Using Leaf Level Hyperspectral Measurements. *Comput. Electron. Agric.* **2012**, *85*, 13–23. [CrossRef]
6. Ashourloo, D.; Mobasheri, M.R.; Huete, A. Developing Two Spectral Disease Indices for Detection of Wheat Leaf Rust (Puccinia-triticina). *Remote Sens.* **2014**, *6*, 4723–4740. [CrossRef]
7. Abdulridha, J.; Ampatzidis, Y.; Roberts, P.; Kakarla, S.C. Detecting Powdery Mildew Disease in Squash at Different Stages Using UAV-Based Hyperspectral Imaging and Artificial Intelligence. *Biosyst. Eng.* **2020**, *197*, 135–148. [CrossRef]
8. Zhou, R.-Q.; Jin, J.-J.; Li, Q.-M.; Su, Z.-Z.; Yu, X.-J.; Tang, Y.; Luo, S.-M.; He, Y.; Li, X.-L. Early Detection of Magnaporthe Oryzae-Infected Barley Leaves and Lesion Visualization Based on Hyperspectral Imaging. *Front. Plant Sci.* **2019**, *9*, 1962. [CrossRef]
9. Guo, A.; Huang, W.; Ye, H.; Dong, Y.; Ma, H.; Ren, Y.; Ruan, C. Identification of Wheat Yellow Rust Using Spectral and Texture Features of Hyperspectral Images. *Remote Sens.* **2020**, *12*, 1419. [CrossRef]
10. Shi, Y.; Huang, W.; González-Moreno, P.; Luke, B.; Dong, Y.; Zheng, Q.; Ma, H.; Liu, L. Wavelet-Based Rust Spectral Feature Set (WRSFs): A Novel Spectral Feature Set Based on Continuous Wavelet Transformation for Tracking Progressive Host–Pathogen Interaction of Yellow Rust on Wheat. *Remote Sens.* **2018**, *10*, 525. [CrossRef]
11. Zhang, J.; Lin, Y.; Wang, J.; Huang, W.; Chen, L.; Zhang, D. Spectroscopic Leaf Level Detection of Powdery Mildew for Winter Wheat Using Continuous Wavelet Analysis. *J. Integr. Agric.* **2012**, *11*, 1474–1484. [CrossRef]
12. Zhao, Y.-R.; Li, X.; Yu, K.-Q.; Cheng, F.; He, Y. Hyperspectral Imaging for Determining Pigment Contents in Cucumber Leaves in Response to Angular Leaf Spot Disease. *Sci. Rep.* **2016**, *6*, 27790. [CrossRef] [PubMed]
13. Martins, G.D.; Galo, M.D.L.B.T.; Vieira, B.S. Detecting and Mapping Root-Knot Nematode Infection in Coffee Crop Using Remote Sensing Measurements. *IEEE J. Sel. Top. Appl. Earth Obs. Remote Sens.* **2017**, *10*, 5395–5403. [CrossRef]
14. Wu, Y.; Zhao, Q.; Yin, X.; Wang, Y.; Tian, W. Multi-Parameter Health Assessment of Jujube Trees Based on Unmanned Aerial Vehicle Hyperspectral Remote Sensing. *Agriculture* **2023**, *13*, 1679. [CrossRef]
15. Liu, Y.; Zhang, Y.; Jiang, D.; Zhang, Z.; Chang, Q. Quantitative Assessment of Apple Mosaic Disease Severity Based on Hyperspectral Images and Chlorophyll Content. *Remote Sens.* **2023**, *15*, 2202. [CrossRef]
16. Ata-Ul-Karim, S.T.; Cao, Q.; Zhu, Y.; Tang, L.; Rehmani, M.I.A.; Cao, W. Non-Destructive Assessment of Plant Nitrogen Parameters Using Leaf Chlorophyll Measurements in Rice. *Front. Plant Sci.* **2016**, *7*, 1829. [CrossRef] [PubMed]
17. Sims, N.C.; De Barro, P.; Newnham, G.J.; Kalyebi, A.; Macfadyen, S.; Malthus, T.J. Spectral Separability and Mapping Potential of Cassava Leaf Damage Symptoms Caused by Whiteflies (*Bemisia tabaci*). *Pest Manag. Sci.* **2018**, *74*, 246–255. [CrossRef] [PubMed]
18. Huang, W.; Guan, Q.; Luo, J.; Zhang, J.; Zhao, J.; Liang, D.; Huang, L.; Zhang, D. New Optimized Spectral Indices for Identifying and Monitoring Winter Wheat Diseases. *IEEE J. Sel. Top. Appl. Earth Obs. Remote Sens.* **2014**, *7*, 2516–2524. [CrossRef]
19. Zarco-Tejada, P.J.; Camino, C.; Beck, P.S.A.; Calderon, R.; Hornero, A.; Hernández-Clemente, R.; Kattenborn, T.; Montes-Borrego, M.; Susca, L.; Morelli, M.; et al. Previsual Symptoms of Xylella Fastidiosa Infection Revealed in Spectral Plant-Trait Alterations. *Nat. Plants* **2018**, *4*, 432–439. [CrossRef]
20. Tian, L.; Xue, B.; Wang, Z.; Li, D.; Yao, X.; Cao, Q.; Zhu, Y.; Cao, W.; Cheng, T. Spectroscopic Detection of Rice Leaf Blast Infection from Asymptomatic to Mild Stages with Integrated Machine Learning and Feature Selection. *Remote Sens. Environ.* **2021**, *257*, 112350. [CrossRef]
21. Zhu, H.; Chu, B.; Zhang, C.; Liu, F.; Jiang, L.; He, Y. Hyperspectral Imaging for Presymptomatic Detection of Tobacco Disease with Successive Projections Algorithm and Machine-Learning Classifiers. *Sci. Rep.* **2017**, *7*, 4125. [CrossRef]
22. Milton, E.J.; Schaepman, M.E.; Anderson, K.; Kneubühler, M.; Fox, N. Progress in Field Spectroscopy. *Remote Sens. Environ.* **2009**, *113*, S92–S109. [CrossRef]
23. Cheng, X.; Feng, Y.; Guo, A.; Huang, W.; Cai, Z.; Dong, Y.; Guo, J.; Qian, B.; Hao, Z.; Chen, G.; et al. Detection of Rubber Tree Powdery Mildew from Leaf Level Hyperspectral Data Using Continuous Wavelet Transform and Machine Learning. *Remote Sens.* **2024**, *16*, 105. [CrossRef]
24. Cerovic, Z.G.; Masdoumier, G.; Ghozlen, N.B.; Latouche, G. A New Optical Leaf-Clip Meter for Simultaneous Non-Destructive Assessment of Leaf Chlorophyll and Epidermal Flavonoids. *Physiol. Plant.* **2012**, *146*, 251–260. [CrossRef]
25. Gitelson, A.A.; Gritz †, Y.; Merzlyak, M.N. Relationships between Leaf Chlorophyll Content and Spectral Reflectance and Algorithms for Non-Destructive Chlorophyll Assessment in Higher Plant Leaves. *J. Plant Physiol.* **2003**, *160*, 271–282. [CrossRef] [PubMed]

26. Gitelson, A.A.; Viña, A.; Ciganda, V.; Rundquist, D.C.; Arkebauer, T.J. Remote Estimation of Canopy Chlorophyll Content in Crops. *Geophys. Res. Lett.* **2005**, *32*, L08403. [CrossRef]

27. Kim, M.S.; Daughtry, C.S.T.; Chappelle, E.W.; McMurtrey, J.E.; Walthall, C.L. The Use of High Spectral Resolution Bands for Estimating Absorbed Photosynthetically Active Radiation (A Par). In Proceedings of the 6th International Symposium on Physical Measurements and Signatures in Remote Sensing, Val D'Isere, France, 17–21 January 1994.

28. Haboudane, D.; Miller, J.R.; Tremblay, N.; Zarco-Tejada, P.J.; Dextraze, L. Integrated Narrow-Band Vegetation Indices for Prediction of Crop Chlorophyll Content for Application to Precision Agriculture. *Remote Sens. Environ.* **2002**, *81*, 416–426. [CrossRef]

29. Daughtry, C.S.; Walthall, C.L.; Kim, M.S.; De Colstoun, E.B.; McMurtrey, J.E., III. Estimating Corn Leaf Chlorophyll Concentration from Leaf and Canopy Reflectance. *Remote Sens. Environ.* **2000**, *74*, 229–239. [CrossRef]

30. Filella, I.; Serrano, L.; Serra, J.; Peñuelas, J. Evaluating Wheat Nitrogen Status with Canopy Reflectance Indices and Discriminant Analysis. *Crop Sci.* **1995**, *35*, 1400–1405. [CrossRef]

31. Penuelas, J.; Frederic, B.; Filella, I. Semi-Empirical Indices to Assess Carotenoids/Chlorophyll-a Ratio from Leaf Spectral Reflectance. *Photosynthetica* **1995**, *31*, 221–230.

32. Blackburn, G.A. Spectral Indices for Estimating Photosynthetic Pigment Concentrations: A Test Using Senescent Tree Leaves. *Int. J. Remote Sens.* **1998**, *19*, 657–675. [CrossRef]

33. Gamon, J.A.; Penuelas, J.; Field, C.B. A Narrow-Waveband Spectral Index That Tracks Diurnal Changes in Photosynthetic Efficiency. *Remote Sens. Environ.* **1992**, *41*, 35–44. [CrossRef]

34. Merzlyak, M.N.; Gitelson, A.A.; Chivkunova, O.B.; Rakitin, V.Y. Non-destructive Optical Detection of Pigment Changes during Leaf Senescence and Fruit Ripening. *Physiol. Plant.* **1999**, *106*, 135–141. [CrossRef]

35. Metternicht, G. Vegetation Indices Derived from High-Resolution Airborne Videography for Precision Crop Management. *Int. J. Remote Sens.* **2003**, *24*, 2855–2877. [CrossRef]

36. Zarco-Tejada, P.J.; Berjón, A.; López-Lozano, R.; Miller, J.R.; Martín, P.; Cachorro, V.; González, M.R.; de Frutos, A. Assessing Vineyard Condition with Hyperspectral Indices: Leaf and Canopy Reflectance Simulation in a Row-Structured Discontinuous Canopy. *Remote Sens. Environ.* **2005**, *99*, 271–287. [CrossRef]

37. Chappelle, E.W.; Kim, M.S.; McMurtrey, J.E. Ratio Analysis of Reflectance Spectra (RARS): An Algorithm for the Remote Estimation of the Concentrations of Chlorophyll A, Chlorophyll B, and Carotenoids in Soybean Leaves. *Remote Sens. Environ.* **1992**, *39*, 239–247. [CrossRef]

38. Rondeaux, G.; Steven, M.; Baret, F. Optimization of Soil-Adjusted Vegetation Indices. *Remote Sens. Environ.* **1996**, *55*, 95–107. [CrossRef]

39. Rouse, J.W.; Haas, R.H.; Schell, J.A.; Deering, D.W. Monitoring Vegetation Systems in the Great Plains with ERTS. In Proceedings of the Third Earth Resources Technology Satellite-1 Symposium, Washington, DC, USA, 10–14 December 1974.

40. Thenkabail, P.S.; Smith, R.B.; De Pauw, E. Hyperspectral Vegetation Indices and Their Relationships with Agricultural Crop Characteristics. *Remote Sens. Environ.* **2000**, *71*, 158–182. [CrossRef]

41. Gitelson, A.; Merzlyak, M.N. Spectral Reflectance Changes Associated with Autumn Senescence of *Aesculus hippocastanum* L. and *Acer platanoides* L. Leaves. Spectral Features and Relation to Chlorophyll Estimation. *J. Plant Physiol.* **1994**, *143*, 286–292. [CrossRef]

42. Gitelson, A.A.; Merzlyak, M.N. Remote Estimation of Chlorophyll Content in Higher Plant Leaves. *Int. J. Remote Sens.* **1997**, *18*, 2691–2697. [CrossRef]

43. Jordan, C.F. Derivation of Leaf-Area Index from Quality of Light on the Forest Floor. *Ecology* **1969**, *50*, 663–666. [CrossRef]

44. Broge, N.H.; Leblanc, E. Comparing Prediction Power and Stability of Broadband and Hyperspectral Vegetation Indices for Estimation of Green Leaf Area Index and Canopy Chlorophyll Density. *Remote Sens. Environ.* **2001**, *76*, 156–172. [CrossRef]

45. Haboudane, D. Hyperspectral Vegetation Indices and Novel Algorithms for Predicting Green LAI of Crop Canopies: Modeling and Validation in the Context of Precision Agriculture. *Remote Sens. Environ.* **2004**, *90*, 337–352. [CrossRef]

46. Merton, R.; Huntington, J. Early Simulation Results of the ARIES-1 Satellite Sensor for Multi-Temporal Vegetation Research Derived from AVIRIS. In Proceedings of the Eighth Annual JPL Airborne Earth Science Workshop, Pasadena, CA, USA, 8–14 February 1999; Citeseer: Princeton, NJ, USA, 1999; pp. 9–11.

47. Zarco-Tejada, P.J.; Miller, J.R.; Mohammed, G.H.; Noland, T.L.; Sampson, P.H. Chlorophyll Fluorescence Effects on Vegetation Apparent Reflectance: II. Laboratory and Airborne Canopy-Level Measurements with Hyperspectral Data. *Remote Sens. Environ.* **2000**, *74*, 596–608. [CrossRef]

48. Zarco-Tejada, P.J.; Miller, J.R.; Mohammed, G.H.; Noland, T.L. Chlorophyll Fluorescence Effects on Vegetation Apparent Reflectance: I. Leaf-Level Measurements and Model Simulation. *Remote Sens. Environ.* **2000**, *74*, 582–595. [CrossRef]

49. Dobrowski, S.Z.; Pushnik, J.C.; Zarco-Tejada, P.J.; Ustin, S.L. Simple Reflectance Indices Track Heat and Water Stress-Induced Changes in Steady-State Chlorophyll Fluorescence at the Canopy Scale. *Remote Sens. Environ.* **2005**, *97*, 403–414. [CrossRef]

50. Sims, D.A.; Gamon, J.A. Relationships between Leaf Pigment Content and Spectral Reflectance across a Wide Range of Species, Leaf Structures and Developmental Stages. *Remote Sens. Environ.* **2002**, *81*, 337–354. [CrossRef]

51. Barnes, J.D.; Balaguer, L.; Manrique, E.; Elvira, S.; Davison, A.W. A Reappraisal of the Use of DMSO for the Extraction and Determination of Chlorophylls a and b in Lichens and Higher Plants. *Environ. Exp. Bot.* **1992**, *32*, 85–100. [CrossRef]

52. Peñuelas, J.; Filella, I.; Biel, C.; Serrano, L.; Savé, R. The Reflectance at the 950–970 Nm Region as an Indicator of Plant Water Status. *Int. J. Remote Sens.* **1993**, *14*, 1887–1905. [CrossRef]

53. Babar, M.A.; Reynolds, M.P.; van Ginkel, M.; Klatt, A.R.; Raun, W.R.; Stone, M.L. Spectral Reflectance to Estimate Genetic Variation for In-Season Biomass, Leaf Chlorophyll, and Canopy Temperature in Wheat. *Crop Sci.* **2006**, *46*, 1046–1057. [CrossRef]

54. Kononenko, I. Estimating Attributes: Analysis and Extensions of RELIEF. In Proceedings of the Machine Learning: ECML-94, Catania, Italy, 6–8 April 1994; Bergadano, F., De Raedt, L., Eds.; Springer: Berlin/Heidelberg, Germany, 1994; pp. 171–182.

55. Li, H.; Liang, Y.; Xu, Q.; Cao, D. Key Wavelengths Screening Using Competitive Adaptive Reweighted Sampling Method for Multivariate Calibration. *Anal. Chim. Acta* **2009**, *648*, 77–84. [CrossRef]

56. Mallat, S. *A Wavelet Tour of Signal Processing*; Elsevier: Amsterdam, The Netherlands, 1999.

57. Mallat, S. Zero-Crossings of a Wavelet Transform. *IEEE Trans. Inf. Theory* **1991**, *37*, 1019–1033. [CrossRef]

58. Torrence, C.; Compo, G.P. A Practical Guide to Wavelet Analysis. *Bull. Am. Meteorol. Soc.* **1998**, *79*, 61–78. [CrossRef]

59. Cheng, T.; Rivard, B.; Sanchez-Azofeifa, A. Spectroscopic Determination of Leaf Water Content Using Continuous Wavelet Analysis. *Remote Sens. Environ.* **2011**, *115*, 659–670. [CrossRef]

60. Vapnik, V. *The Nature of Statistical Learning Theory*; Springer Science & Business Media: Berlin/Heidelberg, Germany, 1999.

61. Karatzoglou, A.; Meyer, D.; Hornik, K. Support Vector Machines in R. *J. Stat. Softw.* **2006**, *15*, 1–28. [CrossRef]

62. Smola, A.J.; Schölkopf, B. A Tutorial on Support Vector Regression. *Stat. Comput.* **2004**, *14*, 199–222. [CrossRef]

63. Breiman, L. Random Forests. *Mach. Learn.* **2001**, *45*, 5–32. [CrossRef]

64. Hosmer, D.W., Jr.; Lemeshow, S.; Sturdivant, R.X. *Applied Logistic Regression*; John Wiley & Sons: Hoboken, NJ, USA, 2013; ISBN 978-0-470-58247-3.

65. Pedregosa, F.; Varoquaux, G.; Gramfort, A.; Michel, V.; Thirion, B.; Grisel, O.; Blondel, M.; Prettenhofer, P.; Weiss, R.; Dubourg, V.; et al. Scikit-Learn: Machine Learning in Python. *J. Mach. Learn. Res.* **2011**, *12*, 2825–2830.

66. Ustin, S.L.; Gitelson, A.A.; Jacquemoud, S.; Schaepman, M.; Asner, G.P.; Gamon, J.A.; Zarco-Tejada, P. Retrieval of Foliar Information about Plant Pigment Systems from High Resolution Spectroscopy. *Remote Sens. Environ.* **2009**, *113*, S67–S77. [CrossRef]

67. Torriani, S.F.F.; Melichar, J.P.E.; Mills, C.; Pain, N.; Sierotzki, H.; Courbot, M. Zymoseptoria Tritici: A Major Threat to Wheat Production, Integrated Approaches to Control. *Fungal Genet. Biol.* **2015**, *79*, 8–12. [CrossRef]

68. Song, L.; Wang, L.; Yang, Z.; He, L.; Feng, Z.; Duan, J.; Feng, W.; Guo, T. Comparison of Algorithms for Monitoring Wheat Powdery Mildew Using Multi-Angular Remote Sensing Data. *Crop J.* **2022**, *10*, 1312–1322. [CrossRef]

69. Guo, A.; Huang, W.; Dong, Y.; Ye, H.; Ma, H.; Liu, B.; Wu, W.; Ren, Y.; Ruan, C.; Geng, Y. Wheat Yellow Rust Detection Using UAV-Based Hyperspectral Technology. *Remote Sens.* **2021**, *13*, 123. [CrossRef]

70. Su, J.; Liu, C.; Hu, X.; Xu, X.; Guo, L.; Chen, W.-H. Spatio-Temporal Monitoring of Wheat Yellow Rust Using UAV Multispectral Imagery. *Comput. Electron. Agric.* **2019**, *167*, 105035. [CrossRef]